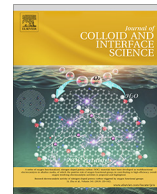




Contents lists available at ScienceDirect

Journal of Colloid and Interface Science

journal homepage: www.elsevier.com/locate/jcis

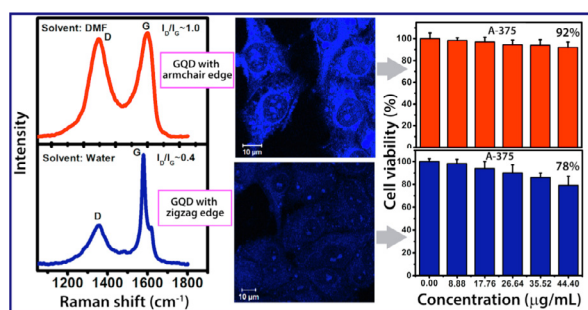
Regular Article

Solvent dependent synthesis of edge-controlled graphene quantum dots with high photoluminescence quantum yield and their application in confocal imaging of cancer cells

Gone Rajender^a, Upashi Goswami^b, P.K. Giri^{a,b,*}^a Department of Physics, Indian Institute of Technology Guwahati, Guwahati 781039, India^b Centre for Nanotechnology, Indian Institute of Technology Guwahati, Guwahati 781039, India

GRAPHICAL ABSTRACT

Control of the edge sites and functional groups of graphene quantum dots using different solvents to yield high photoluminescence quantum yield and its application in confocal imaging of cancer cells.



ARTICLE INFO

Article history:

Received 14 November 2018

Revised 18 January 2019

Accepted 22 January 2019

Available online 23 January 2019

Keywords:

Graphene quantum dots

Edge control

Blue photoluminescence

Bio-imaging

Raman

Thermogravimetric analysis

ABSTRACT

We report on the synthesis of edge-controlled and highly fluorescent few-layer graphene quantum dots (GQDs) using different solvents and explore their application in the confocal imaging of cancer cells. TEM and AFM imaging analysis reveal that GQDs of sizes in the range 5–8 nm and few-layer (1–4) thickness were grown using DMF, DMSO, and water as solvents. Micro-Raman analysis reveals that GQDs grown with DMF possess primarily the armchair edges, while that grown with water contains primarily the zigzag edges. The nature of oxygen functional groups on the edge/in-plane sites of carbon atoms was elucidated through thermogravimetric and FTIR analyses. The GQDs containing high density of armchair edges and oxygen functional group defects exhibited high photoluminescence (PL) quantum yield (~32%). The time-resolved PL measurements suggest the charge transfer from the GQDs to the surrounding dielectric medium. Further, we explore the high PL quantum yield of GQDs in bio-imaging of A-375 and HeLa cancer cells. The cell viability of GQDs on A-375 cells was found to be considerably higher than that of HeLa cells at a GQD concentration of 44.4 μg/mL, which is very significant. Our results indicate the GQD edge site dependent cell viability, for the first time. These results will be useful for the development of highly fluorescent GQDs with specific edge structure and their exploration in the field of bio-imaging, bio-sensing, and drug delivery applications.

© 2019 Elsevier Inc. All rights reserved.

* Corresponding author at: Department of Physics, Indian Institute of Technology Guwahati, Guwahati 781039, India.

E-mail address: giri@iitg.ac.in (P.K. Giri).

1. Introduction

Graphene quantum dots (GQDs) represent an emerging class of zero-dimensional material and it has drawn massive attention due to their bright visible photoluminescence (PL) emission, low toxicity, excellent biocompatibility, and high resistance to photobleaching etc. [1–4]. The tunable and strong PL emission of GQDs is more advantageous than the semiconductor QDs due to its low toxicity and eco-friendly nature [5]. GQDs have been considered as a versatile material and the research on GQDs is exploring to focus on various applications in the fields ranging from optoelectronic, sensors, environmental, supercapacitors to bio-imaging [5–10]. In particular, the bright visible PL emission of GQDs is appealing in applications based on GQD-based sensors, such as immuno-sensors, metal ion catchers, and humidity detectors [11,12], bio-sensing and bio-imaging [8,13]. Top-down methods of synthesis of GQDs include the cutting of carbon materials such as graphene sheets [14,15], carbon fibers [3], multiwalled carbon nanotubes [16], electrolysis of the graphite rod [17], chemical exfoliation of graphite [1], refluxing the XC-72 carbon black in concentrated HNO_3 [18] and activated carbon [19]. However, the PL quantum yields (QY) of the GQDs is often low. The low PL QY limits their further practical applications, in particular in the bio-imaging of cancer cells. The PL emission of GQDs arises mainly from the size effect, edge sites and oxygenated functional group defects in GQDs and mechanism of PL is often explained on the basis of intrinsic states that include the size, edge defects, while the extrinsic defect states correspond to the attachment of functional groups [3,20–23]. Considering the present understanding on the origin of PL of GQDs and its ensuing applications, the effect of solvent on the synthesis and understanding the PL mechanism in different solvents are important for optoelectronic, drug delivery and bio-imaging applications. It is well known that the GQDs are well dispersed in many solvents including water due to the presence of oxygenated functional groups. The solvent dependent PL of GQDs has been reported in the literature [20,24,25]. However, the origin of changes in PL in different liquid media has not been addressed. Note that GQDs are ultra-small fragments of graphene, thus nano-sized GQDs are dominated by edge defects and functional groups around the periphery. It's noteworthy that GQDs offer a particular advantage over the other carbon nanomaterials due to its plenty of edge sites and oxygen functional groups [21,26–29]. Wu et al. [30] studied the comparison of *in vitro* toxicity of graphene oxide (GO) and GQDs on MGC-803 (human gastric cancer) and MCF-7 cells (human breast cancer). It was reported that GO has much higher cytotoxicity than GQDs. In another report, Wang et al. [31] studied the cytotoxicity of GO and nitrogen doped GQDs for red blood cells (RBCs). GO causes apparent cytotoxicity on RBCs than the nitrogen-doped GQDs [31]. Thus, GQDs show excellent bio-compatibility as compared to the GO due to their ultrafine size. In addition, GQDs have been studied in bio-imaging of HeLa [32], A-549 [1], and T47D [3] cell lines. Peng et al. [3] evaluated the cytotoxicity of blue and green fluorescent GQDs using two different human breast cancer cell lines MDAMB-321 and T47D for GQDs concentration up to 50 $\mu\text{g}/\text{mL}$. Although the bio-imaging application of GQDs has been explored, to the best of our knowledge, the bio-imaging on A-375 cells using GQDs has not been studied in the literature.

Herein, we report on the synthesis of edge-controlled and highly fluorescent few-layer (1–4) GQDs using different solvents. In particular, we study the origin of solvent dependent PL spectra of GQDs and its application in the confocal imaging of cancer cells. High-resolution TEM imaging along with the selected area electron diffraction pattern allows us to study the crystal structure of GQDs prepared with different solvents. Raman intensity pattern of GQDs suggests that the nature of edge sites and functional groups in the GQDs are dependent on the nature of solvents used during the syn-

thesis of GQDs. Thermogravimetry analysis is exploited to assess the various oxygenated edge functional groups in GQDs, which is corroborated by the matrix-assisted laser desorption/ionization-time of flight (MALDI-TOF) and FTIR analyses. Our PL studies in liquid media displayed a strong dependence of PL spectra on the solvents, suggesting the definite contribution of surface defect states to the PL spectrum of GQDs. Further, the carrier recombination dynamics was probed by time resolved PL analysis for a better understanding of the PL emission. We report a high 32% PL QY from the GQDs, which is very promising for bio-imaging application. Confocal laser scanning microscopy imaging reveals bright blue luminescence from cancer cells (A-375 and HeLa) and thus confirm the uptake of GQDs by the cancer cells. The concentration dependence of GQDs on bio-compatibility of the cell lines is also assessed and discussed.

2. Experimental details

2.1. Materials and reagents

Expandable graphite flakes were received from the Asbury carbons and NaNO_3 , KMnO_4 , PEG (molecular weight 1500N), quinine sulfate were procured from the Sigma-Aldrich. H_2SO_4 , HNO_3 , H_2O_2 , dimethylformamide (DMF), dimethyl sulfoxide (DMSO), tetrahydrofuran (THF) chemicals were received from Merck. The cancer cell lines A-375 and HeLa are obtained from National Chemical Laboratory, Pune and MTT (3-(4,5-dimethylthiazol-2-yl)-2,5-diphenyltetrazolium bromide) dye was received from the HiMedia. In all the chemical reactions, deionized (DI) water used.

2.2. Synthesis of GQDs and its cell culture

For the synthesis of GQDs, oxidized graphene oxide (OGO) is used as precursor material and DMF, DMSO, and water are used as different solvents. The details of size reduction of GO and synthesis of GQDs are provided in the Supporting Information (Section S1 (a-b)). GQDs synthesized using solvents DMF, DMSO and water are denoted as GQD1, GQD2, GQD3, respectively. GQD3 functionalized with polyethylene glycol (PEG) is labeled as GQD3-F. The cancer cell lines, such as A-375 (human malignant melanoma cells) and HeLa (human cervical carcinoma) were cultured in Dulbecco's modified Eagle's medium supplemented with L-glutamine (4 mM), 10,000 units penicillin, streptomycin (10 mg/mL), and 10% (v/v) fetal bovine serum (obtained from PAA Laboratories, Austria). The cells were incubated in 5% CO_2 humidified incubator at 37 °C.

2.3. Cell viability test

The viability effects of different GQDs on cancer cells lines were assessed by using a MTT dye assay. For this study, 5×10^3 of A-375 cells/well were seeded in a 96-well microtiter plate. Further, these cells were allowed to grow overnight by maintaining the same medium and conditions as discussed in the previous section. Then, GQDs at different concentrations were added in each well in triplicates and incubated for 24 h. Afterwards, MTT dye was added in each well to find out the number of viable cells. The viable cells reduce the yellow tetrazolium MTT by the action of dehydrogenase enzymes, to an insoluble, colored (dark purple) formazan product. The resulting intracellular purple formazan crystals are solubilized in DMSO. The solution has an absorbance (A) peak at 570 nm. A similar procedure was followed for MTT assay studies of HeLa cell lines using different GQDs samples. The % of cell viability was determined by using the following equation.

$$\% \text{ of cell viability} = \frac{(A570 - A655)_{\text{sample}}}{(A570 - A655)_{\text{control}}} \times 100 \quad (1)$$

where the control data was obtained in the absence of GQDs and sample data was obtained in the presence of GQDs. Each experiment was performed three times and the average value is presented. The procedures for preparation of cell lines and GQDs for confocal microscopy imaging and the PL QY measurements are provided in Section S2 and S3 (Supporting Information), respectively.

2.4. Characterization techniques

The morphological features of the GQDs were assessed by high-resolution transmission electron microscopy (HRTEM, JEOL 2100) and selected area electron diffraction (SAED) pattern, operated at 200 kV. The crystalline quality and hexagonal structure of GQDs was studied from X-ray diffraction (XRD) pattern. XRD pattern was recorded with a Rigaku RINT 2500 TTRAX-III using the Cu K_{α} radiation. The micro-Raman spectroscopy measurements were performed using a high-resolution Raman spectrometer (Horiba, LabRam HR) with an excitation wavelength of 488 nm. The excitation source was focused with the 100 \times objective lens giving a spatial resolution of $\sim 1 \mu\text{m}$ and 1 mW of laser power was used to avoid laser heating and damage to the sample. The Raman signal was collected by a CCD in a backscattering geometry sent through a multimode fiber grating of 1800 grooves/mm. The UV–visible absorption spectroscopy measurement was performed with a commercial spectrophotometer (Shimadzu, UV3101PC). PL measurements on GQDs were carried out at room temperature with a commercial fluorimeter (Fluoromax-4, Horiba) with a Xenon lamp source and the samples were excited at 350 nm wavelength. Atomic force microscopy (AFM, Agilent, Model 5500) images were recorded in a non-contact operation mode. Thermogravimetric analysis (TGA) data were obtained with STA7200 HITACHI (Thermal analyzer) with a heating rate of 5 $^{\circ}\text{C}/\text{min}$ by purging the high purity O_2 gas. MALDI-TOF spectrum of GQDs was obtained with a BRUKER instrument (Model: Autoflex speed). Fourier transform infrared (FTIR) spectroscopy measurement was performed with a commercial spectrometer (Perkin Elmer, Spectrum BX). For FTIR measurement, GQDs with KBr powder was mixed and thin circular pellets were prepared by using KBr pellet machine. The confocal microscopy imaging of the cell lines was observed with the commercial fluorescence microscopy (Zeiss LSM 880) with the 405 nm laser excitation. The MTT based assay measurements were performed with a commercial microplate reader (TECAN, Infinite M200 PRO).

3. Results and discussion

3.1. Morphological and structural analysis

The morphological and structural characteristics of the samples were analyzed by TEM including HRTEM, AFM and XRD analyses. In Fig. 1, the first row (a–c) corresponds to the TEM, HRTEM and AFM images of GQD1, respectively; similarly, the second row (d–f) corresponds to GQD2 and the last row (g–i) refers to that of GQD3. The size distribution of GQD1, GQD2, and GQD3 are shown in the insets of Fig. 1(a, d, g), respectively. The mean size of the GQDs grown by using DMF, DMSO and water solvents are 5.3 ± 0.1 , 8.3 ± 0.1 and 5.7 ± 0.1 nm, respectively. These results suggest that the sizes of the GQDs are dependent to some extent on the solvents used during the GQD synthesis. Note that in case of DMF and water solvents the GQDs were synthesized inside a high pressure autoclave at 200 $^{\circ}\text{C}$, while for DMSO the GQDs were synthesized without the autoclave i.e. in an open container. This is due to the higher vapor pressure of DMSO, which did not allow to per-

form the reaction inside an autoclave. The higher average size of GQDs in case of DMSO may be due to the lower/atmospheric pressure during the reaction. The dotted circles in the middle column in Fig. 1 represents the HRTEM lattice images of the GQDs. The calculated lattice spacing values are 0.29, 0.27 and 0.33 nm for GQD1, GQD2, and GQD3, respectively. The first two values corresponding to the (1120) plane and 0.33 nm confirms the (002) planes of sp^2 carbon [4]. Further, the SAED patterns for GQD1, GQD2, and GQD3 shown in the inset of Fig. 1(b, e, h), respectively, suggest the sp^2 arrangement of carbon atoms in GQDs. Fig. 1(c, f, i) shows the AFM images of the GQD1, GQD2, and GQD3, respectively. Each line segment in AFM images and its corresponding height profiles are shown at bottom of the AFM image. AFM height profile analysis suggests that GQD1, GQD2, and GQD3 consists of 1–3, 1–4 and 1–4 layers of graphene, respectively. These results suggest that synthesized GQDs consist of few (1–4) layers of graphene and are good candidates for emerging applications, in particular, the bio-imaging. In addition, to support the sp^2 graphitic frame of the GQDs, we recorded the XRD pattern and the results are shown in Fig. S1 (Supporting Information). Fig. S1(a) shows the XRD pattern of GQD2 and GQD3 in the range $2\theta = 23\text{--}34^{\circ}$. It is evident from the figure that both the samples exhibited the (002) reflection peak, which is a signature of the hexagonal lattice structure of the graphitic material. The (002) XRD peak is a piece of strong evidence for the graphitic structure. The (002) peak center for GQD2 and GQD3 are at $2\theta = 26.34, 26.08^{\circ}$ and their corresponding inter-layer distance (d) are calculated as 3.38 and 3.41 \AA , respectively. The interlayer distance in the present case is slightly different from the graphite value 3.40 \AA [1], which is possibly due to the strain. In addition, the weak reflection peaks at $2\theta \sim 43^{\circ}$ and $\sim 45^{\circ}$ shown in Fig. S1(b) correspond to the (100) and (110) planes, which confirms the in-plane disorder structure in GQDs [33]. The in-plane disorder includes the crystalline defects and oxygen functional groups in the basal plane and these are created/attached during the growth of the GQDs. These results are further confirmed from the micro-Raman analysis, as discussed below.

3.2. Micro-Raman analysis

In order to assess the solvent dependent structural features in GQDs, the micro-Raman measurements on GQDs samples were performed with 488 nm laser excitation. All the GQDs samples show the characteristic Raman bands of graphene, such as G, D, and D'. The Raman G band originates from the in-plane vibrations (E_{2g} mode) of sp^2 carbon [34]. The D band is known to be the disordered band and it signifies the disordered structure of GQDs that is composed of edge sites, crystalline defects, and functional groups. Edge is a kind of the disorder in GQDs, which can be analyzed from its Raman spectra. Note that the D band intensity is very sensitive to the graphene edges [35,36] and it is high for armchair edges and low for zigzag edges [35–37]. The other disorder band, known as D', which is attributed to the vacancies and/or pentagonal and octagonal defects, usually referred to as zigzag 5–7 defects in GQDs [38,39]. In order to get an insight into the nature of edges in the present case, we deconvoluted the Raman spectra of GQDs into D, G, and D' bands. Fig. 2 depicts the deconvoluted Raman spectra of GQD1, GQD2, GQD3, and GQD3-F. We estimate the relative intensities (I) of Raman D and G bands for all the samples. GQD1 synthesized by DMF solvent shows the Raman I_D/I_G ratio of 1.15, while the GQD2 synthesized by DMSO solvent shows a ratio of 0.87 (see Table S1, Supporting Information). Note that the D band intensity is expected to be high for the armchair edges in GQDs. Thus, our results imply that the GQD1 contains a higher density of armchair edges as compared to that of GQD2. The Raman I_D/I_G ratio for GQD3 is 0.37, which signifies the dominance of zigzag edge sites in GQD3 as mentioned in Table 1. Thus, the edge sites of

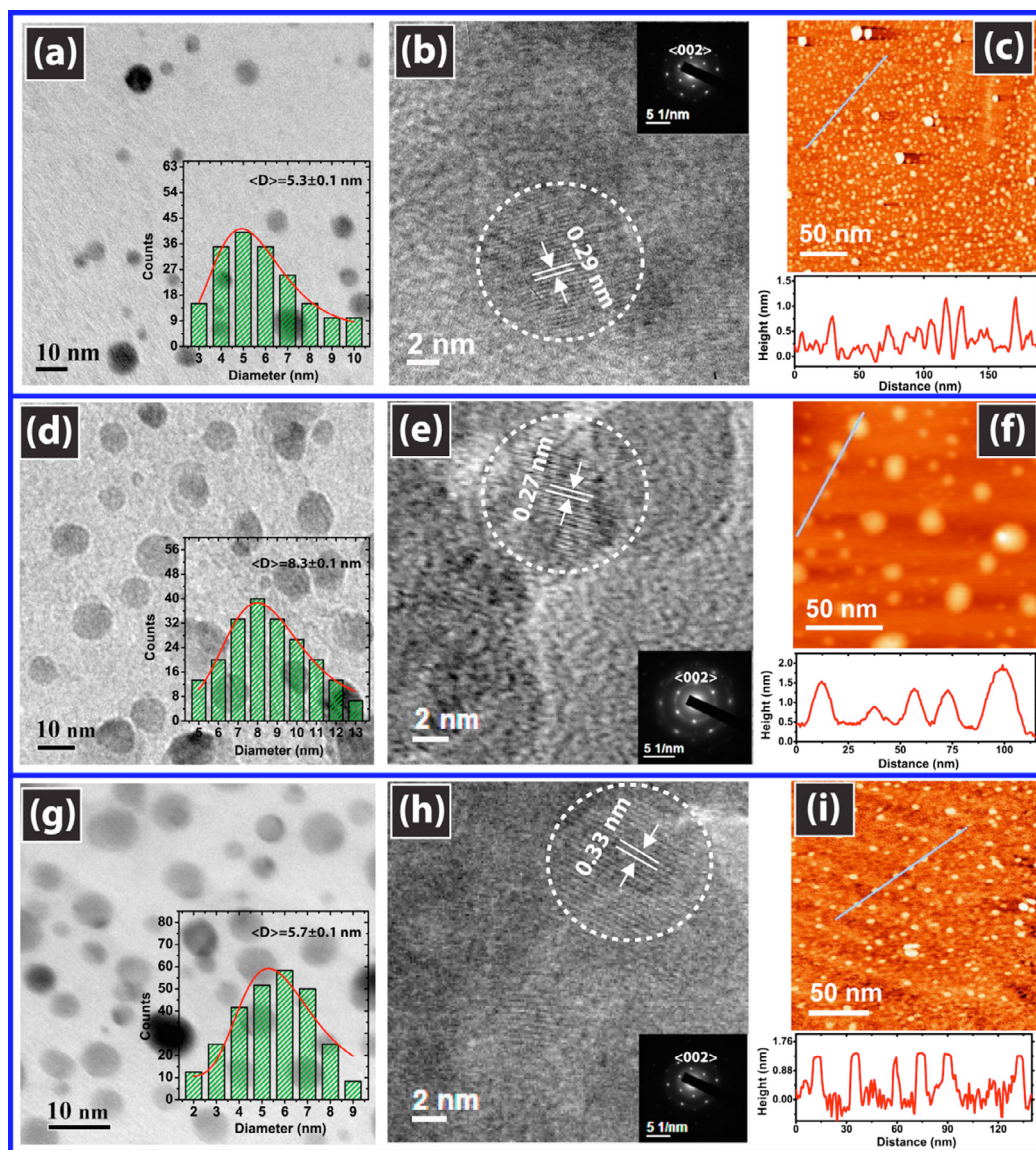


Fig. 1. TEM and AFM imaging analysis of GQDs. TEM, HRTEM and AFM images of GQD1 (a–c), GQD2 (d–f), GQD3 (g–i), respectively. Histograms in (a, d, g) signify the size distribution of GQD1, GQD2, and GQD3, respectively. Average diameter (D) is mentioned in each case. The HRTEM lattice image of each GQD sample is indicated by dotted circles in the middle column. The measured lattice spacing is indicated in each case. Inset in (b, e, h) represents the SAED pattern for the GQDs and it signifies the hexagonal structure of few-layered graphene. A line segment in AFM image and its corresponding height profile are shown at the bottom of the (c, f, i). The GQDs consist of a few (1–4) layers of graphene.

GQDs can be controlled by the solvent chosen for the solvothermal/hydrothermal synthesis. Interestingly, after *in-situ* functionalization of GQD3, the Raman I_D/I_G ratio is increased to 0.53 (GQD3-F). This is because of some of the zigzag edge sites are passivated by the PEG and result in the reduction of zigzag edges. It implies that the chemical functionalization induces the structural changes in GQDs and the GQDs have distinct edge configuration based on preparation conditions. Note that the D' band shown in Fig. 2 is due to the presence of vacancies and/or pentagonal and octagonal defects, usually referred as zigzag 5–7 defects on the basal plane of GQDs [19–21]. The relative intensity ratio of $I_{D'}/I_G$ values for GQD1, GQD2, GQD3, and GQD3-F are 0.58, 0.38, 0.22 and 0.29, respectively. The Raman I_D/I_G values of the samples are provided in Table S1 (Supporting Information). These results imply a higher density of carbon vacancies and/or pentagonal and octagonal defects in the GQD1. Thus, the edge and in-plane defects in the GQDs can be manipulated by using different solvents during the preparation. Our previous report on similar GQDs showed that

the broad D band could be fitted to 3 additional sidebands, ascribed to the sp^2 – sp^3 carbon, COOH/C–OH and C=O/C–O edge oxygen functional groups, respectively [37].

3.3. MALDI-TOF and TGA studies

In order to assess the mass distribution of the synthesized product, we carried out the ion mass spectrum characterization. Fig. 3 (a) shows the MALDI-TOF spectrum of GQD1 and it confirms the fragments of graphene nanostructures [40,41]. The multiple m/z values in the spectrum are significant implying the presence of edges and functional groups in the six-membered poly ring structure of the non-uniform sized GQDs, which is consistent with our conclusion from the Raman results and the literature reports [40–42]. Note that the molecular weight of GQD1 is found to be $\sim 30,000$, which signifies the presence of additional species, such as oxygen functional groups in GQD1. Further, the structural changes of the GQDs due to the attachment of different oxygen

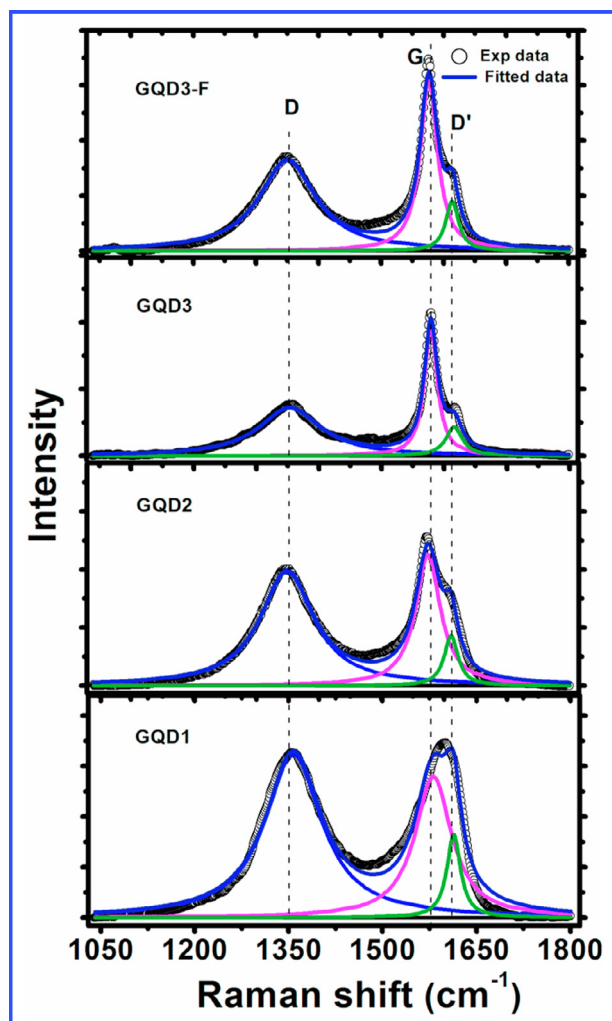


Fig. 2. Deconvoluted Raman spectra of GQD1, GQD2, GQD3, and GQD3-F. The characteristic Raman bands D, G, and D' are labeled in the figure.

functional groups are analyzed by TGA/DTG profiles. Fig. 3(b)–(d) show the TGA/DTG profiles of GQD1, GQD3, and GQD3-F, respectively. In the case of GQD1, the multiple DTG peaks arise due to the loss of different oxygenated functional groups and different

forms of carbon in GQD. First, the low-temperature DTG peaks at 193 and 239, 265 °C suggest the loss of hydroxyl/in-plane epoxy and C–O ether functional groups, respectively, from GQDs [37]. The DTG peaks centered at 276 and 297 °C are due to the loss of COOH related functional groups from GQDs [37]. The other DTG peaks at 352, 466 and 646 °C are due to the loss of C=O related functional groups, sp^3 , and sp^2 carbon, respectively [37,43]. Thus, the GQD1 shows the presence of hydroxyl/in-plane epoxy, C–O ether, COOH and C=O related functional groups in addition to the hexagonal carbon. Fig. 3(c) shows the TGA/DTG profile of GQD3 and here the number of DTG peaks is found to be lesser than that of GQD1. In particular, the low-temperature DTG peak at 193 °C is absent in this case, implying the absence of hydroxyl/C–O epoxy groups in GQD3. The DTG peak at 258 °C is due to the loss of epoxy/C–O (ether) functional group in GQD3. The other two peaks at 319 and 360 °C arise from the edge oxygen functional groups, such as COOH and C=O [37,43]. The DTG peaks at 476 and 715 °C signify the loss of sp^3 and sp^2 carbon domains in GQD3, respectively. Furthermore, to monitor the structural changes during the *in-situ* chemical functionalization of GQDs, we measured the TGA/DTG profiles of GQD3-F and the results are shown in Fig. 3(d). Interestingly, the TGA/DTG profile of GQD3-F exhibited more DTG peaks than those found in GQD3 due to the PEG functionalization. Here, the DTG peaks are slightly modified from GQD3, indicating the attachment of functional groups at a different position of carbon atom in GQDs. The DTG peak at 234 °C is due to the loss of epoxy/C–O (ether) functional group. This suggests that the epoxy/ether functional groups are reduced in GQD3-F as compare to the GQD3. In addition, however, there are major changes in the C=O related functional groups after PEG functionalization. The DTG peak at 324 °C is due to the COOH functional groups as discussed above [37,43]. The additional DTG peaks in the region 340–393 °C are due to the loss of different form of highly stable C=O bonds in quinone, lactone and pyrone groups [44–46]. Note that the quinone, lactone, and pyrone groups are attached at the edges of GQDs. The other two DTG peaks at 488 and 722 °C are attributed to the sp^3 and sp^2 carbon, respectively [37,43]. Note that our MALDI-TOF spectrum of GQD1 suggesting that GQDs consist of edge sites and various oxygen functional groups. A similar observation is expected from the other GQD samples. Note that our Raman analysis in addition to the FTIR and the present TGA results provide strong evidence for the edge sites and oxygen functional groups in GQDs. A summary of the different oxygenated functional groups and different forms of carbon found from the DTG results are shown in Table 1. The difference in the functional groups and edge

Table 1

Summary of edge types (inferred from the Raman analysis) and functional groups and different forms of carbon identified from the TGA/DTG profiles of GQDs.

| Sample Code | Solvent during growth | Dominant edge type | DTG peak (°C) | Identity |
|-------------|------------------------------|--------------------|---------------|--------------------|
| GQD1 | DMF | Armchair | 193 | Hydroxyl/C–O epoxy |
| | | | 239, 265 | C–O ether |
| | | | 276, 297 | COOH |
| | | | 352 | C=O related |
| | | | 466 | sp^3 carbon |
| | | | 646 | sp^2 carbon |
| GQD3 | Water | Zigzag | 258 | C–O ether |
| | | | 319 | COOH |
| | | | 360 | C=O related |
| | | | 476 | sp^3 carbon |
| | | | 715 | sp^2 carbon |
| GQD3-F | Water, PEG functionalization | Armchair/Zigzag | 234 | C–O ether |
| | | | 324 | COOH |
| | | | 340, 350 | C=O related |
| | | | 393 | Quinone/Lactone |
| | | | 488 | sp^3 carbon |
| | | | 722 | sp^2 carbon |

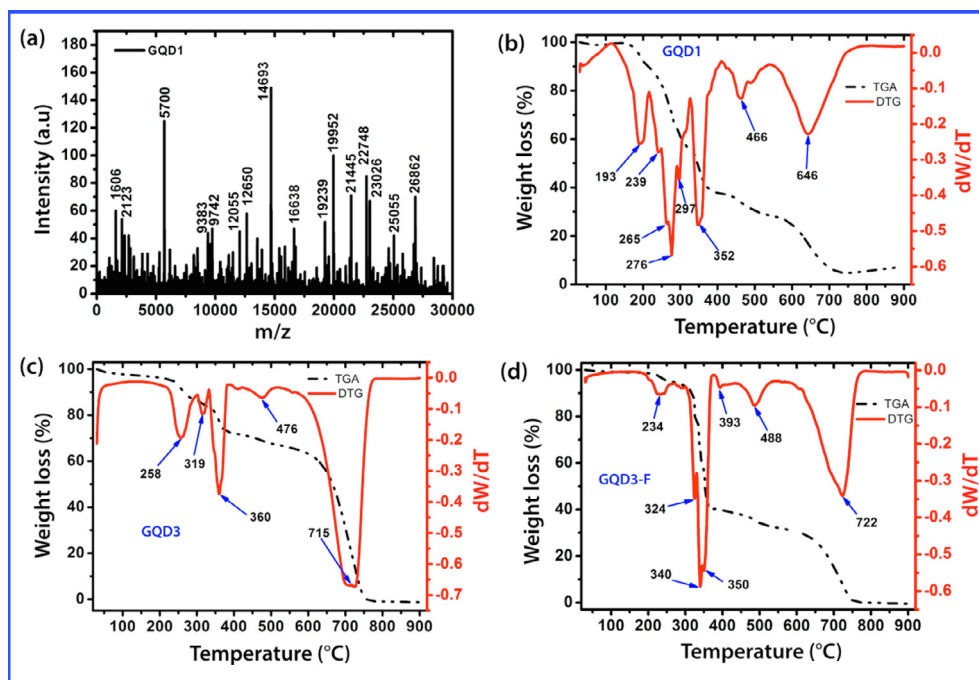


Fig. 3. (a) MALDI-TOF spectrum of GQD1 showing high mass content. (b–d) TGA/DTG profiles of GQD1, GQD3, and GQD3-F, respectively. DTG peak positions ($^{\circ}\text{C}$) are marked in each case.

sites in GQDs prepared with different solvents plays a significant role in the intriguing PL emission from GQDs and bio-imaging of cancer cells, as discussed later.

3.4. FTIR analysis

In order to understand various oxygen functional groups and their attachment at the in-plane and edge sites of GQD, we carried out the FTIR measurement. Fig. 4 shows the characteristic FTIR spectra of GQDs samples. It is evident that various oxygenated functional groups are an attachment and sp^2 carbon network of

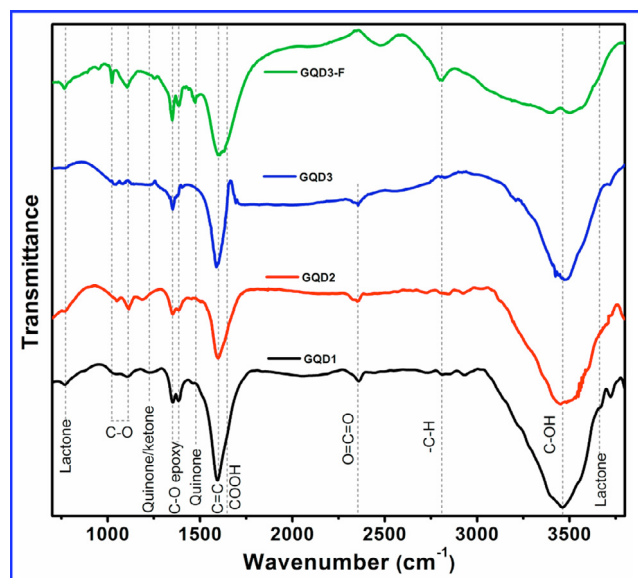


Fig. 4. FTIR spectra of solvent dependent growth of GQDs and their characteristic vibrational modes that are significant for the sp^2 carbon ($\text{C}=\text{C}$) and in-plane, edge oxygenated functional groups of GQDs.

GQDs can be distinguished from the FTIR spectra. The vibrational modes centered at ~ 1024 and $\sim 1106\text{ cm}^{-1}$ are related to the $\text{C}-\text{O}$ stretching vibrations [3]. The other vibrational bands at ~ 1350 and $\sim 1380\text{ cm}^{-1}$ are due to the $\text{C}-\text{O}$ epoxy that is attached to the sp^3 carbon of GQDs [43]. These results are in agreement with TGA/DTG analysis. The strong vibrational mode identified at $\sim 1580\text{ cm}^{-1}$ arises due to the in-plane stretching vibrations of sp^2 hybridized carbon atoms ($\text{C}=\text{C}$) [37,43]. On the other hand, the vibration modes of double bonded oxygen functional groups attached to the edge sites of GQDs, in particularly carboxylic, ketones, lactones, and quinones are evidenced from the FTIR spectra. The vibrational modes at ~ 770 and $\sim 3669\text{ cm}^{-1}$ suggest the lactone functional groups [46]. The peak at $\sim 1650\text{ cm}^{-1}$ in all GQDs is due to the COOH oxygen functional groups [37,43]. The broad peak in the region $\sim 3000\text{--}3800\text{ cm}^{-1}$ signifies the $\text{C}-\text{OH}/\text{OH}$ functional group on the in-plane and edge sites of GQDs [46]. Note that the $\sim 3669\text{ cm}^{-1}$ lactone peak is submerged in the above region. Other vibrational modes identified at ~ 1233 and 1474 cm^{-1} are attributed to the edge oxygen functional groups, such as quinone/ketone and quinone, respectively [46]. Further, some weak bands centered at ~ 2358 and $\sim 2810\text{ cm}^{-1}$ are ascribed to the stretching vibrations of $\text{O}=\text{C}=\text{O}$ and $\text{C}-\text{H}$ modes, respectively [43,46]. Interestingly, the intensity of oxygen functional groups drastically increased in PEG functionalized GQD3-F indicating the effect of *in-situ* chemical functionalization (see Fig. 4). These results are in good agreement with the TGA/DTG analysis discussed in the above section. In addition, the vibrational modes at 1067 , 1104 , 1122 , 1159 , 1237 and 1296 cm^{-1} originate from the single- or bi- vacancies of carbon atom [46]. These defects are formed during the formation of GQDs grown with different solvents. The relative intensity ratio of Raman I_D/I_G suggested some crystal defects (vacancy and SW) in the GQDs samples, as discussed earlier. These results are consistent with TGA/DTG discussed in the above section. Based on the above results of different GQD samples grown using OGO as the precursor and different solvents such as DMF, DMSO, water and *in-situ* PEG functionalization, the growth process for different GQDs is

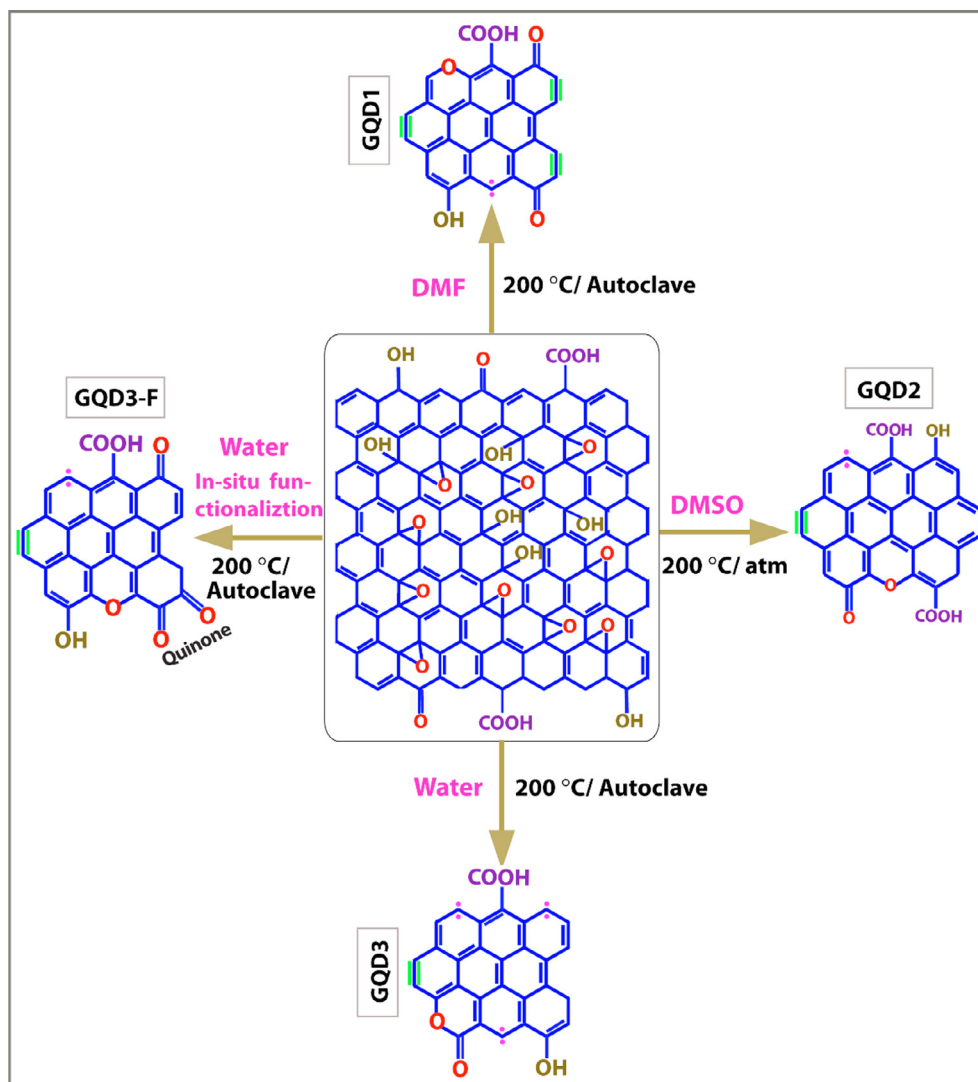


Fig. 5. A schematic illustration of the growth of different types of GQDs from OGO sheets using solvents DMF, DMSO, water and PEG with water. Magenta dots and olive colour bonds refer to the zig-zag and armchair edge sites, respectively. For GQD1, GQD3 and GQD3-F synthesis, reactions were performed inside an autoclave and for GQD2 it was at atmosphere pressure keeping the reaction temperature identical (200 °C) for all the cases. Note that GQD1 contains primarily the armchair edge sites, while GQD3 contains mainly the zig-zag edge sites.

summarized with the help of a schematic diagram, as shown in Fig. 5.

3.5. Optical absorption, PL and time-resolved PL studies

The UV-Vis absorption spectrum of GQD1, GQD2, GQD3, and GQD3-F are shown in Fig. S2 (Supporting Information). All the GQDs samples show the $\pi-\pi^*$ transition (below 300 nm), which is attributed to the sp^2 C=C skeletal framework of carbon domains [4,37,47]. The absorption tail extending from UV (above 300 nm) to visible region signifies the attachment of oxygen functional groups in GQDs and this band is known to be associated with $n-\pi^*$ transition [4,37,47]. Fig. 6 represents PL spectra of four different GQD samples measured in aqueous water. All the GQD samples display the bright blue PL emission. The inset in Fig. 6(a) shows the digital photograph of the GQD aqueous solution excited with 312 nm (Biostep UV transilluminator). All the samples clearly show the PL emission in the blue-green regions. It is clear from the asymmetry of the PL spectrum that multiple peaks contribute to the strong PL emission from the GQDs. To understand the evolution of PL spectra of GQDs synthesized using different solvents, we

deconvoluted each of the PL spectra by the Gaussian peak fitting. Note that each spectrum is fitted with four Gaussian peaks (P1, P2, P3, P4) and different samples show different intensities of these peaks based on the synthesis process. Fig. 6(a–d) depicts the Gaussian peak fitting for GQD1, GQD2, GQD3, and GQD3-F, respectively. Typically, the blue and green emissions from GQDs have been assigned to size confinement, edge defects and functional groups of GQDs [14,20–23,48,49]. Our previous study indicated that the intense PL from GQD thin films primarily originates from the edge sites and oxygen functional groups [37]. The parameters extracted from the fitted Gaussian peaks are tabulated in Table S1 (Supporting Information). Considering the difference in nature of nature of edges in GQD1 and GQD3 as revealed from the Raman analysis, the PL peaks marked at ~ 405 nm (P1), ~ 440 nm (P2) are attributed to the zigzag and armchair edge defects in GQDs, respectively [21,37]. On the other hand, the green PL emission bands centered at ~ 490 nm (P3) and ~ 530 nm (P4) originate from the COOH and C=O related oxygen functional group defects in GQDs [22,37]. Considering the case of GQD1, the PL intensity as well as the FWHM of peak P2 is much higher than that of peak P1, indicating the dominance of armchair edge sites in GQD1 (see Table S1). The other two

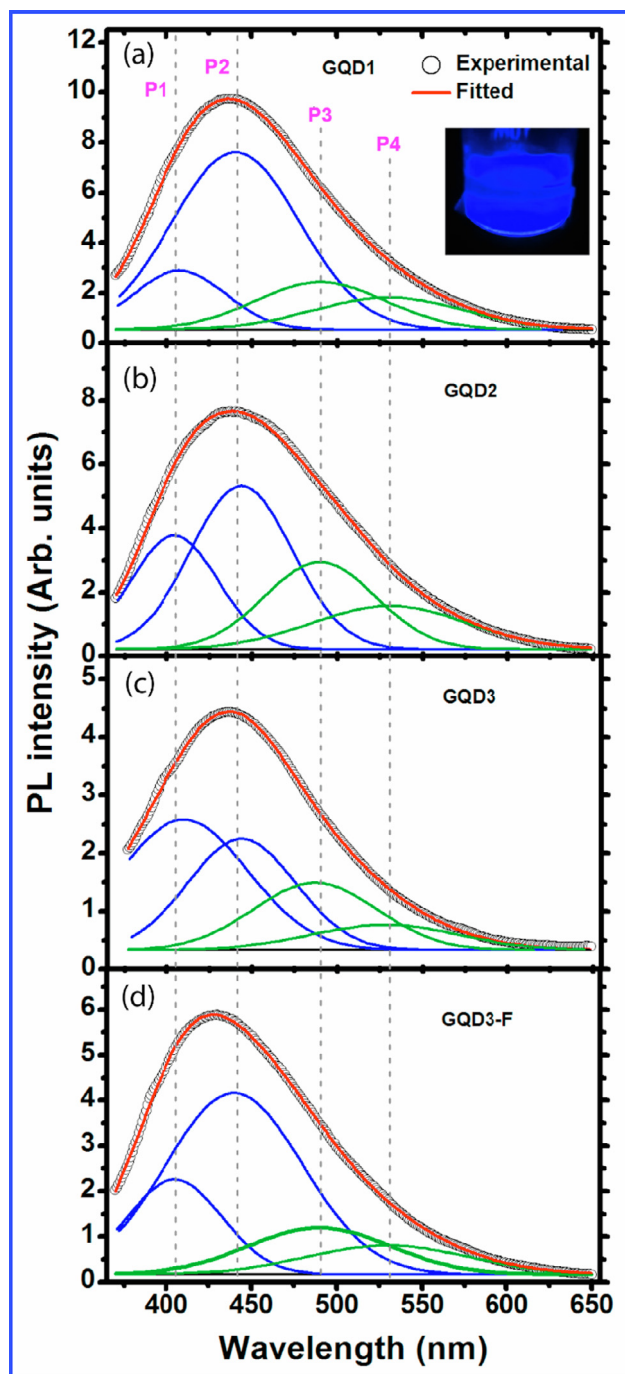


Fig. 6. Comparison of the PL characteristics of different GQD samples. Gaussian fitting of the PL peaks (solid lines) for (a) GQD1, (b) GQD2, (c) GQD3 and (d) GQD3-F. Four peaks (P1-P4) are fitted in each case. Peaks P1 and P2 are assigned to zig-zag and armchair edges, respectively, in GQDs (see text). The inset in (a) shows the digital photograph of the GQDs in water solution under UV light illumination.

peaks, P3 and P4, have lower intensity than that of P2 (see Table S1), implying less dominant role of oxygen functional groups in GQD1. Further, the relative intensity of peak P1 with respect to peak P2 is much higher (~ 5 times) in GQD3 than that of GQD1 (see Table S1), which is consistent with the high concentration of zigzag edge sites in GQD3. These results are fully consistent with the Raman analysis, which shows nearly 3 times lower intensity of D band in GQD3 (see Table S1, Supporting Information) due to low density of armchair edges in it. Similarly, the P3 and P4 are related to the oxygen functional groups defects in GQD2. Next, we com-

pare the fitting parameters of peaks P1-P4 for GQD3 before and after functionalization. There are significant changes in PL intensity in GQD3 before and after functionalization (GQD3-F). For GQD3, the intensity of peak P1 is relatively high compared to other samples, implying the dominance of the zigzag edge sites in GQD3. However, after functionalization, the intensity of peak P1 is reduced, while that of P2 is increased (see Fig. 6(c, d) and Table S1). This is due to the fact that functionalization reduces the zig-zag edge sites in GQD3-F by passivating the sites and thus the peak P1 intensity is reduced. The functionalization may also induce conversion of edge type from zig-zag to arm chair type and as a result the peak P2 intensity is increased in GQD3-F. Thus the interpretation of our PL results is fully consistent with Raman analysis and functionalization experiment. To evaluate the ambient stability of the highly fluorescent GQDs, we measured the PL spectra of GQDs stored in ambient condition after several months. Fig. S3 (Supporting Information) shows the comparative PL spectra of as-grown GQD1 and that after seven months. The data clearly shows that the synthesized GQDs are quite stable under ambient condition for a prolonged duration. Our results clearly reveal that the edge sites and functional groups defects in GQDs can be tuned through the solvent dependent synthesis and *in-situ* functionalization.

The origin of PL from GQDs is reported to be due to the size confinement, edge sites and functional group defects [14,20–23,48,49]. Despite sustainable efforts in understanding the origin of PL from GQDs, the exact mechanism remains unclear. Our previous study indicated that the intense PL from GQD thin films primarily originates from the edge sites and oxygen functional groups [37]. The present study provides further evidence for surface state dependent PL emission from GQDs. In order to prove the surface state dependent PL emission from GQDs, we performed the PL measurements in different solvents having different dielectric constants (ϵ). Fig. 7(a) shows a comparison of the normalized PL spectra of GQD3 in water, DMSO and THF solvents. Interestingly, the spectral blue shift is noticeable for the GQD3 dispersed in DMSO, thus confirming its dependence on the dispersing media. This is possibly due to the reactive sites in GQDs; edges and oxygen functional groups of GQD initiates the interaction with the solvent. Note that the edge sites and oxygen functional groups have the free electrons at the carbon edges and they influence the recombination dynamics. The line width of the PL in the solvent can be explained on the basis of dielectric media of the solvent. In the case of the THF, it has a dielectric constant value of $\epsilon = 7.58$, smaller than that of water ($\epsilon = 80$) and DMSO ($\epsilon = 47$). The lower line width of the PL spectra in THF could be due to efficient charge transfer from GQDs to solvent. Since THF has low dielectric constant and GQDs are enriched with edge sites and functional groups, the solvation process is faster than the fluorescence [50]. This result is consistent with the TRPL analysis (discussed below). The shift of the PL peak of GQDs in different solvents indicates that the surface states of GQDs strongly contribute to the visible PL emission.

In order to ascertain the charge transfer process of GQDs in solvents, we measured the lifetime of carriers in GQDs using the TRPL measurements. Fig. 7(b) shows the TRPL spectra of GQD3 in DMSO and THF. The TRPL spectra are well fitted with the tri-exponential decay equation [7]. The carrier lifetimes and their amplitudes are summarised in Table S2 (Supporting Information). The three different lifetimes can be attributed to the recombination of electrons from the edge sites and functional groups defects in GQDs [7,17,51]. The average lifetime of the carrier in GQD3 dispersed in DMSO is 6.74 ns, while it reduces to 3.84 ns in case of THF. As discussed above, since the THF has lower dielectric constant than the DMSO, during the light irradiation the charge from enriched edges and functional groups of GQDs is transferred to the THF through the solvation process [50]. This shorter lifetime of carriers

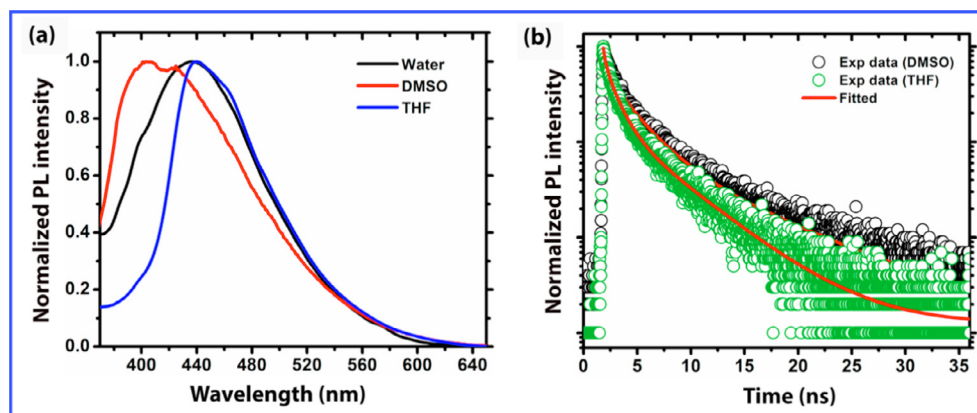


Fig. 7. (a) Comparison of the PL spectra of GQD3 measured in different solvents. (b) Comparison of the TRPL decay profiles of GQD3 measured in DMSO and THF.

in THF solvent indicates the efficient charge transfer from GQDs to THF.

For a quantitative assessment of PL emission of GQDs, the QY of GQDs is measured by using the quinine sulfate (QS) as a standard dye, having QY of 0.54. The PL QY for the GQD1, GQD2, GQD3, and GQD3-F are found as 32%, 27%, 15%, and 21%, respectively. The details absorbance, PL integrated intensity and the QY of different GQDs are presented in Table 2. Among all the GQDs, the GQD1 shows highest PL QY of 32%, which can be attributed due to the enriched armchair edges and additional oxygen functional groups. Note that the *in-situ* chemical functionalization showed improved PL QY (in GQD3-F) as compared to the bare GQD3. The reported PL QY of GQDs synthesis by DMF solvent and GO precursor is $\sim 17.4\%$ [23,24,52]. Thus, we achieved nearly double PL QY than the reported value for our GQD sample. A summary of the reported PL QY of the GQDs synthesized by different top-down methods and precursor materials is listed in Table S3 (Supporting Information). To the best of our knowledge, we report here the highest PL QY of GQDs made using the DMF solvent starting with the oxidized GO as a precursor material. Note that we adopted an optimum reaction temperature and pressure (inside autoclave) based on the TGA/DTG results to form the GQDs with high PL QY. Our results showed that in addition to the armchair edge defects (in GQD1), oxygen functional groups are also responsible for the improved PL QY. High QY implies higher radiative recombination and lower non-radiative recombination channels in the GQDs, consistent with the TRPL analysis.

3.6. Cell viability and bio-imaging studies

The bright blue PL emission of GQDs was exploited in studying the confocal imaging of cancer cells at high spatial resolution. Prior to the confocal imaging of cells using GQDs as fluorescent markers, the viability of A-375 and HeLa cells was analyzed in presence of different GQDs with the help of MTT assay. The cell viability of GQD1, GQD2, GQD3, and GQD3-F was evaluated with varied

concentration from 0 to 44.4 $\mu\text{g}/\text{mL}$ on A-375 and HeLa for 24 h. The cell viability results of the four GQDs samples on these cell lines are portrayed in Fig. 8(a–d). Fig. 8(a) shows the comparison of cell viability with the GQD1 on A-375 and HeLa cells after 24 h of treatment with the GQD concentration in the range 0–44.4 $\mu\text{g}/\text{mL}$. The cell viabilities of A-375 and HeLa cells with GQD1 are found to be 92% and 78%, respectively, at a concentration of 44.4 $\mu\text{g}/\text{mL}$, indicating that the GQD1 has considerably higher cell viability in A-375 cells. Fig. 8(b) shows the comparison of cell viability of the GQD2 for the concentration of 0–44.4 $\mu\text{g}/\text{mL}$ on the A-375 and HeLa cells and respective cell viabilities are 90% and 80%. Further, the cell viability of GQD3 and GQD3-F on A-375 and HeLa is shown in Fig. 8(c) and (d), respectively. The GQD3 treated cells, 79% of cells are viable for both A-375 and HeLa cells. On the other hand, at 26.64 $\mu\text{g}/\text{mL}$ concentration, GQD-F shows 92% cell viability on HeLa cells, whereas 85% of A-375 cells were viable and with further increasing its concentration up to 44.4 $\mu\text{g}/\text{mL}$ both the cell lines shows 81% of viability. These results indicate that edge sites and selective functionalization of GQDs could tune the bio-compatibility of GQDs over the cancer cell lines. Our results suggest that the highly photoluminescent GQDs shows good bio-compatibility on cancer cells. In particular, the high viability of GQD1 for A-375 cell (92%) is very significant and reported here for the first time. Note that despite their similar sizes, the nature of edge states in GQD1 (armchair) and GQD3 (zigzag) are very different and the content of the functional group is higher in GQD1 than that in GQD3. Since GQD1 shows higher cell viability than GQD3, we believe that the armchair edges and the oxygenated functional groups both help in having higher cell viability in A-375 cell. Thus, one can tune the cell viability of GQDs by tuning its size, edge structure, and functional groups defects. These results are very significant for future application of GQDs in *in-vitro* imaging of cancer cells. Finally, our results indicate that the as-prepared GQDs are nontoxic to both the cell lines up to 44.4 $\mu\text{g}/\text{mL}$ concentration and thus useful for high-resolution imaging of cancer cells.

Considering the excellent bio-compatibility of GQDs on A-375 and HeLa cells, we carried out the confocal imaging of the cells using GQDs as a labeling agent. For this, confocal imaging was carried out for different GQDs samples on HeLa and A-375 cells. Fig. 9 shows bright field and fluorescence images of the A-375 and HeLa cell lines by using GQD1 and GQD2. Fig. 8(a, b) and (e, f) shows the confocal images of A-375 and HeLa cell lines, respectively, when GQD1 is used as the biomarker. Similarly, Fig. 9(c, d) and (g, h) shows the confocal images of A-375 and HeLa cell lines, respectively, when GQD2 is used as the labeling agent. The first and third columns represent the bright field images, while the second and fourth columns represent the fluorescence images. Confocal microscopy images of A-375 cells and HeLa cells with GQD3 and GQD3-F

Table 2
Summary of absorbance, integrated PL intensity and PL QY of different GQD samples.

| Sample Code | Absorbance (at 350 nm) | Integrated PL intensity (10^6 counts) | PL QY (%) |
|-------------|------------------------|--|---------------------------|
| QS | 0.013 | 19.64 | 54.0 ± 0.2 (Standard) |
| GQD1 | 0.023 | 20.60 | 32.0 ± 0.2 |
| GQD2 | 0.015 | 11.34 | 27.0 ± 0.2 |
| GQD3 | 0.010 | 4.19 | 15.0 ± 0.2 |
| GQD3-F | 0.030 | 17.64 | 21.0 ± 0.2 |

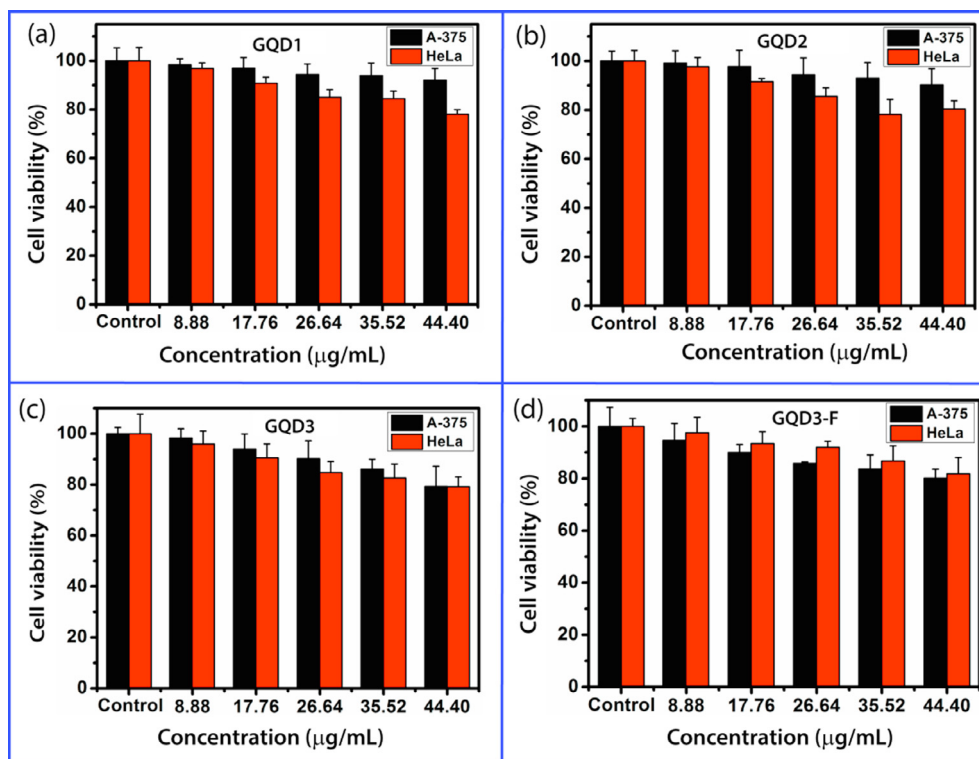


Fig. 8. Comparison of cell viability of A-375 and HeLa cell lines with GQDs samples; (a) GQD1, (b) GQD2, (c) GQD3 and (d) GQD3-F. For A-375 cell, GQD1 shows the highest cell viability (92%), while GQD3 shows the lowest (79%).

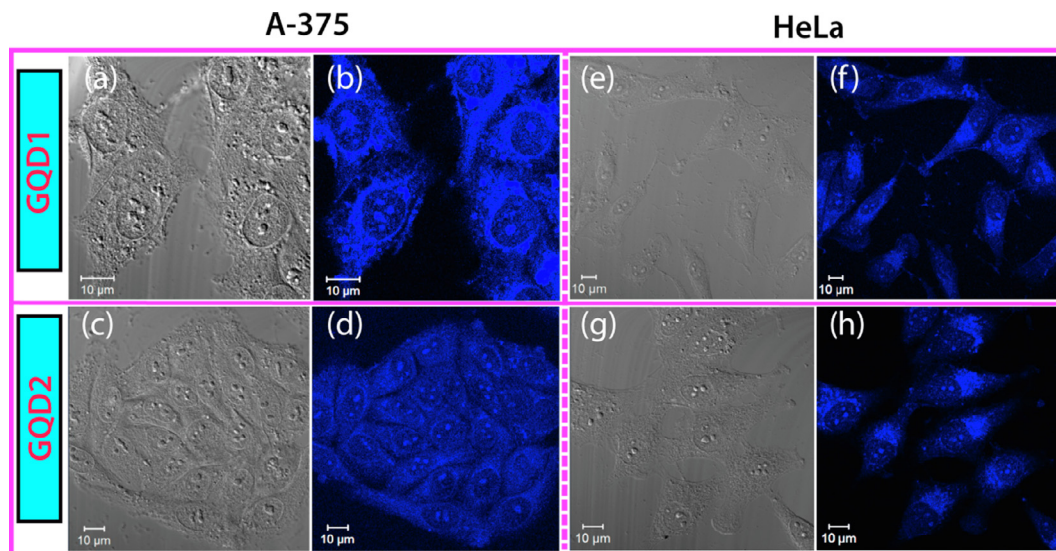


Fig. 9. Laser confocal microscopy images of GQDs inside the cancer cells. A-375 cells imaging by (a, b) GQD1 and (c-d) GQD2; HeLa cells imaging by (e, f) GQD1 and (g, h) GQD2. The 1st and 3rd columns correspond to the bright field images and the 2nd and 4th columns correspond to fluorescence images of the cells.

are provided in Fig. S4 (Supporting Information). In each case, the bright blue luminescence is observed inside the cells, indicating that the GQDs have been internalized by the A-375 and HeLa cells and are mainly localized in the cytoplasm region (see Fig. 9 and Fig. S4). To confirm its internalization, the cells were treated with GQDs for 4 h and we recorded the confocal Z-stack images, as depicted in Fig. S5 (Supporting Information). Fig. S5(a) shows the confocal Z-stack image of A-375 cell lines by GQD1, while Fig. S5 (b) shows the Z-stack image for the same cell lines using GQD3. It is evident from Fig. S5 that GQDs are internalized inside cell

lines, however, GQD1 is more up taken in A-375 cell lines as compared to the GQD3. This result is consistent with the cytotoxicity of GQD1 and GQD3 in A-375 cell line (see Fig. 8(a, c)). The confocal imaging of HeLa cell lines (control sample) without any addition of GQDs is shown in Fig. S6. The uptake mechanism of GQDs in both the cell lines is believed to occur by GQDs entering through the endocytosis process [53,54]. Due to the small sizes, the uptake is high, particularly for GQD1. Further studies may be needed to pinpoint the understanding on the endocytosis internalization of GQDs in the cell lines. These results prove that the strong blue PL

emission, with low cytotoxicity, and ease of labeling of cells with QDs enables its promising applications for biological imaging, disease diagnosis, and bio-sensing.

3.7. Conclusions

In conclusion, the present study focused on the solvent dependent synthesis of edge controlled and highly fluorescent few layer QDs. The high PL yield of QDs was employed to study the bio-imaging of cancer cells. Our studies suggested that the edge sites and functional groups of the QDs can be tuned by using different solvents during the top-down synthesis of QDs. TGA/DTG analyses reveal the various oxygenated edge functional groups in QDs and these results along with FTIR analysis allowed us to distinguish and assign the various oxygenated functional groups in QDs. We elucidated the origin of tuneable PL emission from QDs in different liquid media and it is shown that the strong PL emission of QDs arises from the distinct edge sites and functional groups attached to QDs. We achieved a high 32% PL QY from the QDs synthesized using DMF solvent, which is believed to result from the enriched edge sites and oxygen functional groups defects in QDs. The efficiency of PL emission from QDs in the solvent medium depends on its dielectric constant and we probed the charge transfer process from the TRPL analysis. Bio-imaging of cancer cell lines by the QDs revealed bright blue PL emission inside the cancer cell lines, indicating that QDs are an excellent candidate for bio-imaging applications. Cell viability studies indicate very high biocompatibility of as-prepared QDs with A-375 cells as compared to that of HeLa cells. These results are significant for the manipulation of the edge sites and oxygen functional groups defects of QDs and its applications in bio-imaging, sensing and drug delivery to specific sites.

Acknowledgment

We acknowledge central instruments facility, IIT Guwahati for the Raman, TEM, AFM and MALDI-TOF characterization and Centre for Energy, IIT Guwahati for TGA characterizations. Financial support from MEITY (Grant No. 5(9)/2012-NANO (VOL-II)) is gratefully acknowledged.

Appendix A. Supplementary material

Supplementary data to this article can be found online at <https://doi.org/10.1016/j.jcis.2019.01.099>.

References

- [1] Y. Sun, S. Wang, C. Li, P. Luo, L. Tao, Y. Wei, G. Shi, Large scale preparation of graphene quantum dots from graphite with tunable fluorescence properties, *PCCP* 15 (2013) 9907–9913.
- [2] L. Keheng, Z. Xinna, W. Gang, S. Zhiqiang, Recent advances in the cancer bioimaging with graphene quantum dots, *Curr. Med. Chem.* 25 (2018) 2876–2893.
- [3] J. Peng, W. Gao, B.K. Gupta, Z. Liu, R. Romero-Aburto, L. Ge, L. Song, L.B. Alemany, X. Zhan, G. Gao, S.A. Vithayathil, B.A. Kaiparettu, A.A. Marti, T. Hayashi, J.-J. Zhu, P.M. Ajayan, Graphene quantum dots derived from carbon fibers, *Nano Lett.* 12 (2012) 844–849.
- [4] G.W. Lingling Li, Guohai Yang, Juan Peng, Jianwei Zhao, J Focusing on luminescent graphene quantum dots: current status and future perspectives, *Nanoscale* 5 (2013) 4015–4039.
- [5] Z. Wang, H. Zeng, L. Sun, Graphene quantum dots: versatile photoluminescence for energy, biomedical, and environmental applications, *J. Mater. Chem. C* 3 (2015) 1157–1165.
- [6] G. Rajender, J. Kumar, P.K. Giri, Interfacial charge transfer in oxygen-deficient TiO₂-graphene quantum dot hybrid and its influence on the enhanced visible light photocatalysis, *Appl. Catal. B* 224 (2018) 960–972.
- [7] R. Gone, C. Biswajit, P.K. Giri, In situ decoration of plasmonic Au nanoparticles on graphene quantum dots-graphitic carbon nitride hybrid and evaluation of its visible light photocatalytic performance, *Nanotechnology* 28 (2017) 395703.
- [8] Z. Fan, S. Li, F. Yuan, L. Fan, Fluorescent graphene quantum dots for biosensing and bioimaging, *RSC Adv.* 5 (2015) 19773–19789.
- [9] X. Li, M. Rui, J. Song, Z. Shen, H. Zeng, Carbon and graphene quantum dots for optoelectronic and energy devices: a Review, *Adv. Funct. Mater.* 25 (2015) 4929–4947.
- [10] Z. Su, H. Shen, H. Wang, J. Wang, J. Li, G.U. Nienhaus, L. Shang, G. Wei, Motif-designed peptide nanofibers decorated with graphene quantum dots for simultaneous targeting and imaging of tumor cells, *Adv. Funct. Mater.* 25 (2015) 5472–5478.
- [11] H. Sun, L. Wu, W. Wei, X. Qu, Recent advances in graphene quantum dots for sensing, *Mater. Today* 16 (2013) 433–442.
- [12] S. Zhou, H. Xu, W. Gan, Q. Yuan, Graphene quantum dots: recent progress in preparation and fluorescence sensing applications, *RSC Adv.* 6 (2016) 110775–110788.
- [13] K. Li, W. Liu, Y. Ni, D. Li, D. Lin, Z. Su, G. Wei, Technical synthesis and biomedical applications of graphene quantum dots, *J. Mater. Chem. B* 5 (2017) 4811–4826.
- [14] D. Pan, J. Zhang, Z. Li, M. Wu, Hydrothermal route for cutting graphene sheets into blue-luminescent graphene quantum dots, *Adv. Mater.* 22 (2010) 734–738.
- [15] D. Pan, L. Guo, J. Zhang, C. Xi, Q. Xue, H. Huang, J. Li, Z. Zhang, W. Yu, Z. Chen, Z. Li, M. Wu, Cutting sp²clusters in graphene sheets into colloidal graphene quantum dots with strong green fluorescence, *J. Mater. Chem.* 22 (2012) 3314–3318.
- [16] L. Lin, S. Zhang, Creating high yield water soluble luminescent graphene quantum dots via exfoliating and disintegrating carbon nanotubes and graphite flakes, *Chem. Commun.* 48 (2012) 10177–10179.
- [17] M. Zhang, L. Bai, W. Shang, W. Xie, H. Ma, Y. Fu, D. Fang, H. Sun, L. Fan, M. Han, C. Liu, S. Yang, Facile synthesis of water-soluble, highly fluorescent graphene quantum dots as a robust biological label for stem cells, *J. Mater. Chem.* 22 (2012) 7461–7467.
- [18] Y. Dong, C. Chen, X. Zheng, L. Gao, Z. Cui, H. Yang, C. Guo, Y. Chi, C.M. Li, One-step and high yield simultaneous preparation of single- and multi-layer graphene quantum dots from CX-72 carbon black, *J. Mater. Chem.* 22 (2012) 8764–8766.
- [19] Y. Huang, C. Bai, K. Cao, Y. Tian, Y. Luo, C. Xia, S. Ding, Y. Jin, L. Ma, S. Li, Chaos to order: an eco-friendly way to synthesize graphene quantum dots, *RSC Adv.* 4 (2014) 43160–43165.
- [20] S. Zhu, J. Zhang, S. Tang, C. Qiao, L. Wang, H. Wang, X. Liu, B. Li, Y. Li, W. Yu, X. Wang, H. Sun, B. Yang, Surface chemistry routes to modulate the photoluminescence of graphene quantum dots: from fluorescence mechanism to up-conversion bioimaging applications, *Adv. Funct. Mater.* 22 (2012) 4732–4740.
- [21] K. Lingam, R. Podila, H. Qian, S. Serkiz, A.M. Rao, Evidence for edge-state photoluminescence in graphene quantum dots, *Adv. Funct. Mater.* 23 (2013) 5062–5065.
- [22] G. Sandeep Kumar, R. Roy, D. Sen, U.K. Ghorai, R. Thapa, N. Mazumder, S. Saha, K.K. Chattopadhyay, Amino-functionalized graphene quantum dots: origin of tunable heterogeneous photoluminescence, *Nanoscale* 6 (2014) 3384–3391.
- [23] S. Zhu, J. Zhang, X. Liu, B. Li, X. Wang, S. Tang, Q. Meng, Y. Li, C. Shi, R. Hu, B. Yang, Graphene quantum dots with controllable surface oxidation, tunable fluorescence and up-conversion emission, *RSC Adv.* 2 (2012) 2717–2720.
- [24] J. Zhang, Y.-Q. Ma, N. Li, J.-L. Zhu, T. Zhang, W. Zhang, B. Liu, Preparation of graphene quantum dots and their application in cell imaging, *J. Nanomater.* 2016 (2016) 9.
- [25] L. Feng, X.-Y. Tang, Y.-X. Zhong, Y.-W. Liu, X.-H. Song, S.-L. Deng, S.-Y. Xie, J.-W. Yan, L.-S. Zheng, Ultra-bright alkylated graphene quantum dots, *Nanoscale* 6 (2014) 12635–12643.
- [26] K.A. Ritter, J.W. Lyding, The influence of edge structure on the electronic properties of graphene quantum dots and nanoribbons, *Nat. Mater.* 8 (2009) 235–242.
- [27] L.R. Radovic, B. Bockrath, On the chemical nature of graphene edges: origin of stability and potential for magnetism in carbon materials, *J. Am. Chem. Soc.* 127 (2005) 5917–5927.
- [28] M.A. Montes-Morán, D. Suárez, J.A. Menéndez, E. Fuente, On the nature of basic sites on carbon surfaces: an overview, *Carbon* 42 (2004) 1219–1225.
- [29] M. Hassan, E. Haque, K.R. Reddy, A.I. Minett, J. Chen, V.G. Gomes, Edge-enriched graphene quantum dots for enhanced photo-luminescence and supercapacitance, *Nanoscale* 6 (2014) 11988–11994.
- [30] C. Wu, C. Wang, T. Han, X. Zhou, S. Guo, J. Zhang, Insight into the cellular internalization and cytotoxicity of graphene quantum dots, *Adv. Healthcare Mater.* 2 (2013) 1613–1619.
- [31] T. Wang, S. Zhu, X. Jiang, Toxicity mechanism of graphene oxide and nitrogen-doped graphene quantum dots in RBCs revealed by surface-enhanced infrared absorption spectroscopy, *Toxicol. Res.* 4 (2015) 885–894.
- [32] Q. Liu, B. Guo, Z. Rao, B. Zhang, J.R. Gong, Strong two-photon-induced fluorescence from photostable, biocompatible nitrogen-doped graphene quantum dots for cellular and deep-tissue imaging, *Nano Lett.* 13 (2013) 2436–2441.
- [33] M.S. Seehra, V. Narang, U.K. Geddam, A.B. Stefaniak, Correlation between X-ray diffraction and Raman spectra of 16 commercial graphene-based materials and their resulting classification, *Carbon* 111 (2017) 380–385.
- [34] A.C. Ferrari, D.M. Basko, Raman spectroscopy as a versatile tool for studying the properties of graphene, *Nat. Nano* 8 (2013) 235–246.
- [35] L.G. Cançado, M.A. Pimenta, B.R.A. Neves, M.S.S. Dantas, A. Jorio, Influence of the atomic structure on the raman spectra of graphite edges, *Phys. Rev. Lett.* 93 (2004) 247401.

- [36] C. Casiraghi, A. Hartschuh, H. Qian, S. Piscanec, C. Georgi, A. Fasoli, K.S. Novoselov, D.M. Basko, A.C. Ferrari, Raman spectroscopy of graphene edges, *Nano Lett.* 9 (2009) 1433–1441.
- [37] G. Rajender, P.K. Giri, Formation mechanism of graphene quantum dots and their edge state conversion probed by photoluminescence and Raman spectroscopy, *J. Mater. Chem. C* 4 (2016) 10852–10865.
- [38] K.N. Kudin, B. Ozbas, H.C. Schniepp, R.K. Prud'homme, I.A. Aksay, R. Car, Raman spectra of graphite oxide and functionalized graphene sheets, *Nano Lett.* 8 (2008) 36–41.
- [39] S. Claramunt, A. Varea, D. López-Díaz, M.M. Velázquez, A. Cornet, A. Cirera, The importance of interbands on the interpretation of the Raman spectrum of graphene oxide, *J. Phys. Chem. C* 119 (2015) 10123–10129.
- [40] T. Željko, W.M. D. M. Klaus, Superphenalene-based columnar liquid crystals, *Angew. Chem. Int. Ed.* 43 (2004) 755–758.
- [41] T. Fan, W. Zeng, W. Tang, C. Yuan, S. Tong, K. Cai, Y. Liu, W. Huang, Y. Min, A.J. Epstein, Controllable size-selective method to prepare graphene quantum dots from graphene oxide, *Nanoscale Res. Lett.* 10 (2015) 55.
- [42] W. Zhang, Z. Chen, B. Yang, X.-Y. Wang, R. Berger, A. Narita, G.B. Barin, P. Ruffieux, R. Fasel, X. Feng, H.J. Räder, K. Müllen, Monitoring the on-surface synthesis of graphene nanoribbons by mass spectrometry, *Anal. Chem.* 89 (2017) 7485–7492.
- [43] R.K. Biroju, G. Rajender, P.K. Giri, On the origin and tunability of blue and green photoluminescence from chemically derived graphene: hydrogenation and oxygenation studies, *Carbon* 95 (2015) 228–238.
- [44] A. Lerf, H. He, M. Forster, J. Klinowski, Structure of graphite oxide revisited, *J. Phys. Chem. B* 102 (1998) 4477–4482.
- [45] E. Fuente, J.A. Menéndez, M.A. Díez, D. Suárez, M.A. Montes-Morán, Infrared spectroscopy of carbon materials: a quantum chemical study of model compounds, *J. Phys. Chem. B* 107 (2003) 6350–6359.
- [46] M. Acik, G. Lee, C. Mattevi, A. Pirkle, R.M. Wallace, M. Chhowalla, K. Cho, Y. Chabal, The role of oxygen during thermal reduction of graphene oxide studied by infrared absorption spectroscopy, *J. Phys. Chem. C* 115 (2011) 19761–19781.
- [47] D. Qu, M. Zheng, L. Zhang, H. Zhao, Z. Xie, X. Jing, R.E. Haddad, H. Fan, Z. Sun, Formation mechanism and optimization of highly luminescent N-doped graphene quantum dots, *Sci. Rep.* 4 (2014) 5294.
- [48] T.-F. Yeh, W.-L. Huang, C.-J. Chung, I.T. Chiang, L.-C. Chen, H.-Y. Chang, W.-C. Su, C. Cheng, S.-J. Chen, H. Teng, Elucidating quantum confinement in graphene oxide dots based on excitation-wavelength-independent photoluminescence, *J. Phys. Chem. Lett.* 7 (2016) 2087–2092.
- [49] S. Kim, S.W. Hwang, M.-K. Kim, D.Y. Shin, D.H. Shin, C.O. Kim, S.B. Yang, J.H. Park, E. Hwang, S.-H. Choi, G. Ko, S. Sim, C. Sone, H.J. Choi, S. Bae, B.H. Hong, Anomalous behaviors of visible luminescence from graphene quantum dots: interplay between size and shape, *ACS Nano* 6 (2012) 8203–8208.
- [50] S.K. Cushing, M. Li, F. Huang, N. Wu, Origin of strong excitation wavelength dependent fluorescence of graphene oxide, *ACS Nano* 8 (2014) 1002–1013.
- [51] S. Zhu, J. Shao, Y. Song, X. Zhao, J. Du, L. Wang, H. Wang, K. Zhang, J. Zhang, B. Yang, Investigating the surface state of graphene quantum dots, *Nanoscale* 7 (2015) 7927–7933.
- [52] R. Tian, S. Zhong, J. Wu, W. Jiang, Y. Shen, W. Jiang, T. Wang, Solvothermal method to prepare graphene quantum dots by hydrogen peroxide, *Opt. Mater.* 60 (2016) 204–208.
- [53] M.K. Kumawat, M. Thakur, R.B. Gurung, R. Srivastava, Graphene quantum dots for cell proliferation, nucleus imaging, and photoluminescent sensing applications, *Scientific Reports* 7 (2017) 15858.
- [54] W. Shang, X. Zhang, M. Zhang, Z. Fan, Y. Sun, M. Han, L. Fan, The uptake mechanism and biocompatibility of graphene quantum dots with human neural stem cells, *Nanoscale* 6 (2014) 5799–5806.